Nuclear Inst. and Methods in Physics Research, A 907 (2018) 169–181

Contents lists available at ScienceDirect

Nuclear Inst. and Methods in Physics Research, A

journal homepage: www.elsevier.com/locate/nima

Sub-femtosecond precision timing synchronization systems

Ming Xin [a,b,*], Kemal Şafak [a,c], Michael Y. Peng [b], Patrick T. Callahan [b], Aram Kalaydzhyan [a], Wenting Wang [a], Katia Shtyrkova [b], Qing Zhang [a], Shih-Hsuan Chia [a], Briana Jones [d], Todd Hawthorne [d], Philip Battle [d], Oliver D. Mücke [a,c], Tony Roberts [d], Franz X. Kärtner [a,b,c]

[a] *Center for Free-Electron Laser Science, Deutsches Elektronen-Synchrotron, Hamburg 22607, Germany*
[b] *Research Laboratory of Electronics, Massachusetts Institute of Technology, Cambridge, MA 02139, USA*
[c] *Department of Physics and the Hamburg Center for Ultrafast Imaging, University of Hamburg, Hamburg 22761, Germany*
[d] *AdvR Inc., 2310 University Way, Bozeman, MT 59715, USA*

ARTICLE INFO

Keywords:
Optical synchronization techniques
Attosecond photonics
Large-scale timing distribution
Laser–microwave network
Free electron laser
Integrated balanced optical cross correlator

ABSTRACT

We present a timing synchronization system that can synchronize optical and microwave signals with attosecond-level precision across kilometer distances. With this technique, the next-generation photon science facilities like X-ray free-electron lasers and intense laser beamlines can be enabled to observe ultra-fast dynamics in atoms, molecules and condensed matter taking place on an attosecond time scale. We discuss some key technologies including master-laser jitter characterization, local one-color laser synchronization, remote two-color laser synchronization, and analyze technical noise contributions in the system. A 4.7-km laser–microwave network with 950-attosecond timing jitter is realized over tens of hours of continuous operation. Finally, an integrated balanced optical cross correlator is introduced. With the same input power level, the required operational power for each timing link is significantly reduced.

1. Introduction

Timing synchronization is widely used in many aspects of modern science and technology such as congestion resolution in intelligent transportation systems [1], time codes in film making [2], MIDI clock in electronic music [3], and signal modulation/demodulation in coherent optical communication systems [4]. The timing precision of such synchronization techniques ranges from several seconds to a few picoseconds; and maintaining this precision is a prerequisite to make our world more harmonious and more beautiful. With the ever increasing demands, higher timing precision at the femtosecond (fs) and even attosecond (as) level has recently become desirable in photonic-based analog-to-digital converters [5], laser-based inertial confinement fusion [6], fiber-laser accelerators [7], and other advanced applications. Furthermore, achieving such high synchronization precision in large-scale networks can enable new explorations in the near future. For example, fs/as-precision synchronization among telescope arrays [8–12] at hundreds-of-km scale may enable 10^{-6} arcsecond angular resolution (corresponding to 50 km spatial resolution at 1-light-year distance), which is necessary to obtain the surface details of distant astronomical objects. In addition, an atomic-clock-based gravitational waves detector [13,14] with attosecond or even sub-attosecond precision synchronized clock network may greatly increase the detection possibility compared to the current techniques of the Laser Interferometer Gravitational-Wave Observatory (LIGO) [15,16].

Besides these applications discussed above, large-scale fs/as-precision synchronization is most urgently required in free-electron lasers (FELs). Recently, several X-ray FELs (XFELs), such as the European XFEL [17] in Hamburg, FERMI [18] in Italy, SwissFEL in Switzerland and Linac Coherent Light Source (LCLS) [19] and LCLS II [20] in Stanford, are built or being built worldwide with lengths ranging from a few hundred meters to several kilometers. All these facilities aim to generate attosecond X-ray pulses [21] with unprecedented brightness to film physical and chemical reactions with sub-atomic-level spatio-temporal resolution [22,23]. Significant progress in attosecond-level molecule techniques, including the time-domain observation of intramolecular charge transfer [24] and the discovery of ultrafast Auger processes altering the chemistry of matter on an attosecond time scale [25,26], has been made in the past few years. However, the current XFELs are still not using their full potential to capture sub-atomic-level movies due to the lack of an attosecond-precision timing control to avoid blurring of the individual pictures in time. As illustrated in Fig. 1 [27], in order to generate attosecond X-ray pulses and perform attosecond-precision

---

[*] Corresponding author at: Research Laboratory of Electronics, Massachusetts Institute of Technology, Cambridge, MA 02139, USA.
E-mail address: xinm@mit.edu (M. Xin).

https://doi.org/10.1016/j.nima.2017.12.040
Received 30 September 2017; Accepted 12 December 2017

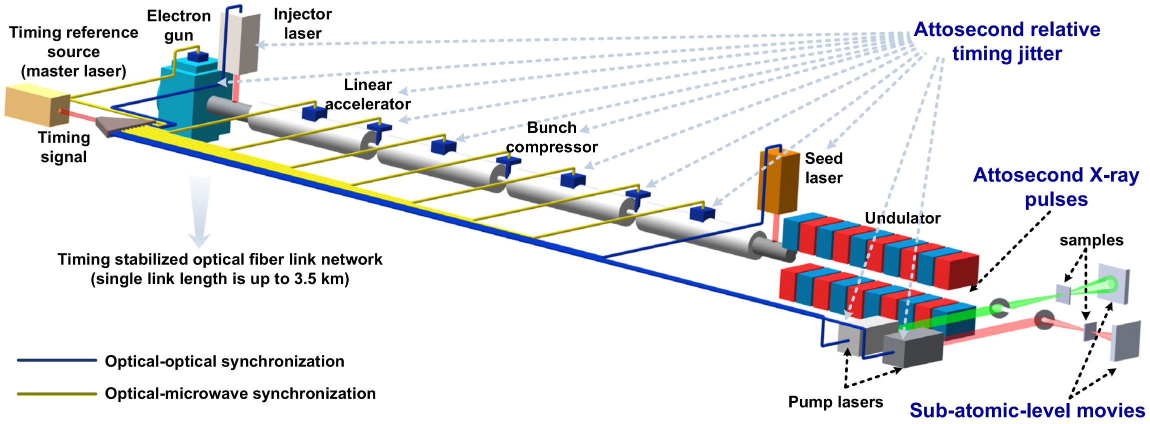

Fig. 1. Timing synchronization system in an attosecond XFEL [27].

pump–probe experiments, all the optical/microwave sub-sources inside an XFEL, including the electron gun, injector laser, microwave references of the linear accelerator and bunch compressor, seed laser and pump lasers at the end station, need to be synchronized simultaneously with attosecond relative timing jitter. Therefore, a multi-km attosecond-precision synchronization technique is imperative to unleash the full potential of these billion-dollar photon-science facilities.

Generally, a timing synchronization system consists of a reference providing extremely stable timing signals, a target signal that needs to be synchronized, a detector that can measure the timing difference between the target signal and the reference, and a control box to lock the timing of the target to that of the reference. If the target device is far away from the reference, a timing link is also necessary to deliver the timing signal from the reference to the target. Without exception, the attosecond-precision synchronization technique also requires these key elements.

The timing reference source in attosecond synchronization can be an atomic clock [28,29], a continuous-wave (CW) laser [30,31] or a mode-locked laser [32,33]. The state-of-the-art technique in each solution can provide an attosecond-jitter-equivalent instability for 1 s observation time. In contrast to the other two solutions, a mode-locked laser can simultaneously provide ultralow-noise optical and microwave signals, and the ultrashort optical pulses in time domain can be directly used as time markers for precise timing measurements. So it is an ideal timing source for synchronization applications such as telescope arrays and XFELs, where the target devices are mode-locked lasers and microwave sources.

Another advantage of using mode-locked lasers is that it can provide very high sensitivity during timing detection, thanks to its high pulse peak power. For example, we have developed balanced optical cross-correlators (BOCs) [34,35] and balanced optical–microwave phase detectors (BOMPDs) [36,37] for optical–optical and optical–microwave timing detection, respectively. Both of them can achieve attosecond precision and >1-ps dynamic range at the same time. In contrast, it is difficult to build comparable timing detectors with atomic clocks or CW laser sources, due to their single-frequency limitation.

Usually the control box can be realized by a feedback loop, which needs to be carefully designed to avoid any feedback-induced noise. For remote synchronization, the timing link can be either optical fiber [38–43] or free space [44,45]. Free-space-based links are limited by the ground buildings and also suffer from atmospheric turbulences. However, it may be suitable for space applications such as gravitational wave detection. Optical-fiber-based timing links, on the other hand, are very flexible for installation and can be easily fitted into telescope arrays and XFELs.

In this work, we focus on the XFEL application, since it possesses currently the most urgent timing challenge. But the techniques we present here can also easily be adapted to other applications in the future. Based on the discussions above, the best synchronization solution for XFELs, as depicted in Fig. 1, should use a mode-locked laser (master laser) as the timing reference, and optical fiber links to distribute the timing signals to different remote laser/microwave sources. We have been working on this approach over the past decade [40] and already breached the 10-fs precision level [46–48], which is more than an order-of-magnitude better than the best results achieved with traditional microwave signal distribution schemes [49,50]. In order to meet the strict timing requirements of XFELs, a novel sub-fs-precision timing synchronization system is developed based upon our previous work, and presented in this paper. In Section 2, we first show the timing jitter characterization of the master laser. Then local synchronization of a 1550 nm laser and remote synchronization of a titanium:sapphire (Ti:Sa) laser are reported in Sections 3 and 4. The technical noise sources of the system are discussed in Section 5, and a 4.7-km laser–microwave network with attosecond precision is presented in Section 6. Finally, an integrated BOC with an unprecedented timing precision is introduced.

2. Master-laser jitter characterization

Since the master laser in Fig. 1 serves as timing reference for all optical/microwave sub-sources, it must exhibit attosecond-level timing jitter, which needs to be accurately characterized. In conventional jitter characterization of mode-locked lasers, the laser output is first detected by a photodetector, and then the phase noise is converted into an amplitude change by a mixer [51] for baseband power spectrum measurement. This scheme, which is adopted by state-of-the-art signal source analyzers (SSAs), suffers from amplitude-to-phase (AM–PM) noise conversion during photodetection [52,53]. Here we use a different characterization method based on BOC [54,55], which is intrinsically immune to AM–PM noise conversion by directly converting the timing difference of two optical pulses into a voltage signal. The BOC characterization has achieved extremely low noise floors down to 10^{-12} $\mathrm{fs}^2/\mathrm{Hz}$ for offset frequencies up to the Nyquist frequency of mode-locked lasers [33,56].

The master-laser jitter characterization setup is shown in Fig. 2. The output of two identical lasers (master and slave, with 216.667 MHz repetition rate, 50 mW average power, 170 fs pulse width and 1553 nm center wavelength) were combined by a polarization beam splitter (PBS) and launched into a BOC, which consists of a single 4-mm-long periodically-poled $\mathrm{KTiOPO_4}$ (PPKTP) crystal operating in a double-pass configuration with appropriate dichroic beam splitter and mirror (DBS, DM) and a low-noise balanced photodetector (BPD). The BOC output was fed back to the piezoelectric transducer (PZT) of the slave laser (with a sensitivity of 17.4 Hz/V) through a proportional–integral (PI) controller so that the two lasers' repetition rates were locked to each other. Finally, the BOC output was sent to an SSA for jitter characterization.

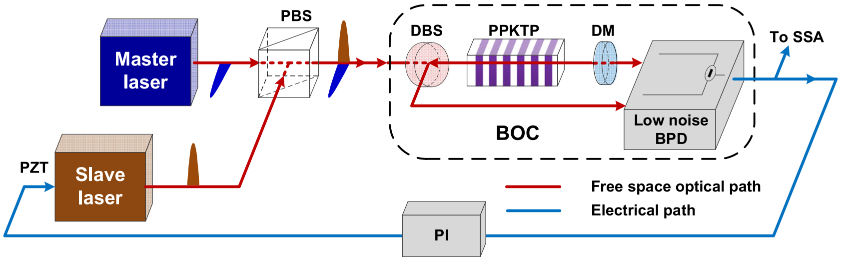

Fig. 2. Master-laser jitter characterization setup (PBS, polarization beam splitter; DBS, dichroic beam splitter; DM, dichroic mirror; PPKTP, periodically-poled KTiOPO$_4$; PI, proportional–integral controller; BPD, balanced photodetector; PZT, piezoelectric transducer; SSA, signal source analyzer).

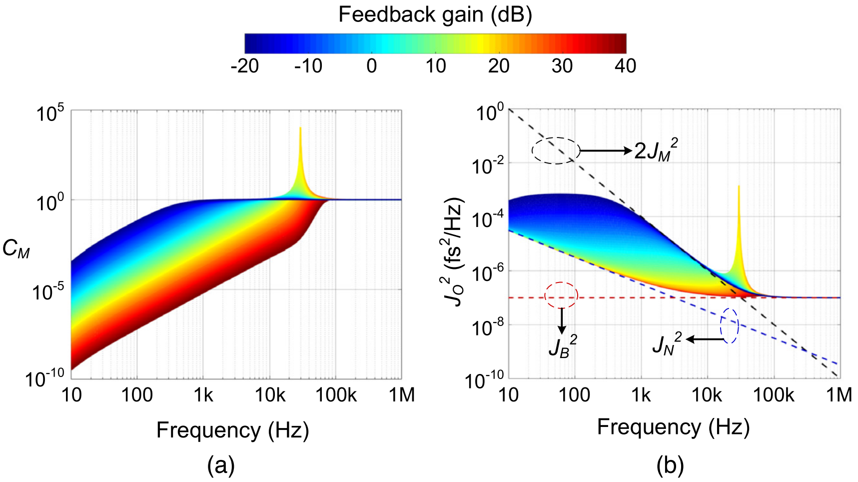

Fig. 3. (a) Coefficient C_M at different feedback gain values; (b) Simulated BOC output jitter spectral density at different feedback gain values. The peaks around 30 kHz in (a) and (b) originate from the PZT resonance of the slave laser. (For interpretation of the references to color in this figure legend, the reader is referred to the web version of this article.)

Based on the BOC locking model in [47,48], the timing jitter spectral density at the output of the BOC satisfies:

$$\overline{J_O^2} = 2C_M\overline{J_M^2} + C_N\overline{J_N^2} + \overline{J_B^2} \tag{1}$$

where $C_M = |1/(1+H)|^2$, $C_N = |H/(1+H)|^2$, H is the total complex transfer function of the feedback loop, J_M is the free-running jitter of the master laser, the factor 2 stems from the assumption that the master and slave lasers have identical but uncorrelated jitter, J_N is the electronic noise from the feedback loop, and J_B is the BPD noise directly coupled into the SSA. In order to use the measured value J_O to estimate J_M, we should let $H \approx 0$. Then $C_M \approx 1$, $C_N \approx 0$, an upper limit estimation of J_M can be given:

$$\overline{J_M^2} \approx \frac{1}{2}\overline{J_O^2} - \frac{1}{2}C_N\overline{J_N^2} - \frac{1}{2}\overline{J_B^2} \le \frac{1}{2}\overline{J_O^2}. \tag{2}$$

Using the feedback parameters from the experiments, we calculate C_M at different feedback gain values, as shown in Fig. 3(a). When the gain is at −20 dB, C_M is almost 1 above 1 kHz. Furthermore, in Fig. 3(b), we assume that J_M^2 has a $1/f^2$ slope (black dashed line), J_N^2 has a $1/f$ slope (blue dashed line) and J_B^2 is a constant (red dashed line), so that we can easily analyze how each noise source affects J_O. It can be seen that as feedback gain increases, J_O approaches J_N from 10 Hz to 1 kHz, and above 50 kHz, J_O is always limited by J_B since J_B dominates the noise sources. While below 50 kHz, more and more low-frequency components of J_O^2 coincide with $2J_M^2$ when the gain decreases. So in terms of measurement, we can decrease the feedback gain as much as possible (e.g., to −20 dB), then we can obtain the accurate master-laser jitter between 1 kHz and 20 kHz and an upper limit estimate above this frequency range.

The master laser characterization results are displayed in Fig. 4. The top panel shows the jitter spectral density at different feedback gains. As predicted by the simulations, the jitter spectrum is limited by the detector noise floor (gray curve) above 30 kHz. Between 1 kHz and 30 kHz, as the gain decreases, the spectrum approaches the real laser jitter. We choose the lowest gain value (about −15 dB) at which the locking is still stable enough to perform a measurement, and obtain 330 as integrated timing jitter from 1 kHz to 1 MHz, as shown in the bottom panel of Fig. 4. This value gives a very good upper limit estimate of the master laser's jitter. So this laser is definitely capable of providing the reference in an attosecond-precision timing synchronization system.

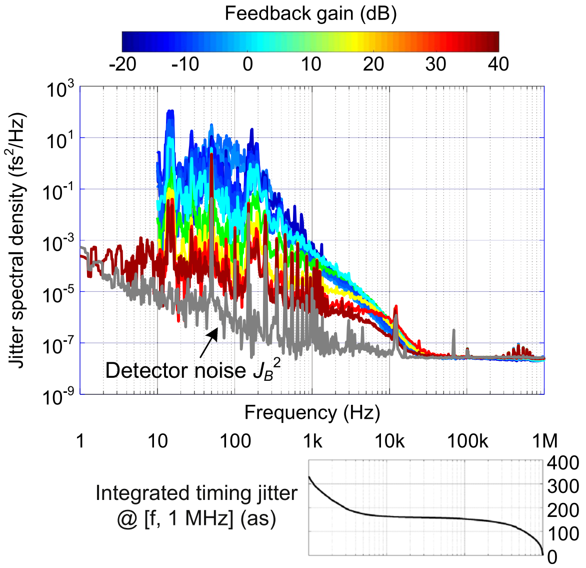

Fig. 4. Measured master-laser jitter spectrum and corresponding integrated timing jitter.

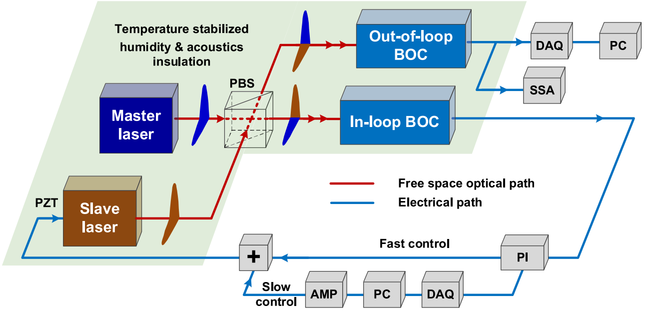

Fig. 5. Local optical–optical synchronization (DAQ, data acquisition card; PC, computer, AMP, voltage amplifier; +, voltage summer).

3. Local 1550 nm laser synchronization

After characterizing the master-laser jitter, it is necessary to test its local synchronization performance before installing it in a distributed network. The local optical–optical synchronization experimental setup is shown in Fig. 5. Similar to that in laser characterization, the repetition rates of the slave and master lasers were first locked together with an in-loop BOC, then another out-of-loop BOC was used to evaluate the jitter performance after synchronization. Both of the two BOCs have the same structure as that shown in Fig. 2. In the feedback loop, the output of the in-loop BOC was first filtered by a PI controller. Then the PI output was separated into two paths: the first path was directly sent to the slave laser's PZT without amplification to compensate fast jitter above 10 Hz; the second path was sampled by a data acquisition (DAQ) card, analyzed by a Labview program to generate a DC voltage to compensate slow jitter below 10 Hz, and a voltage amplifier was used to extend the compensation range. This feedback design can effectively optimize the locking bandwidth and compensation range simultaneously.

To minimize the thermally-induced timing fluctuations, the two lasers, two BOCs and other free-space optics were mounted on a temperature-stabilized breadboard with a Super-Invar surface sheet. With temperature fluctuations controlled below ±0.05 K, the effective timing instability of free-space beam paths due to thermal expansion is only ±1 as/cm. Lead foam was placed beneath the setup to damp table vibrations. A two-layer enclosure with acoustic heavy foil for the inner layer and high-density polyethylene (HDPE) for the outer layer was built to provide acoustic isolation for all optical components. A humidity insulation material covering the outer enclosure was also used to protect the setup from environmental humidity changes.

Fig. 6(a) shows the out-of-loop jitter spectrum from 1 Hz to 1 MHz. The total integrated jitter over this frequency range is only 450 as. A long-term drift measurement was taken and the peak-to-peak drift in 10 h is 400 as, which gives a root-mean-square (RMS) drift of 71 as (Fig. 6(b)). The Fourier transform of the drift data is also calculated in Fig. 6(c). The integrated drift from 200 μHz to 1 Hz is only 50 as. These results indicate that optical synchronization using BOC can easily achieve attosecond precision. Furthermore, they also provide a precision limit that we can approach in the remote timing synchronization.

4. Remote synchronization of a Ti:Sa laser

In order to investigate the jitter noise limitations in the timing synchronization system, we built a Ti:Sa laser synchronization setup on a 4.7-km timing link network [57], as shown in Fig. 7. The reason for choosing the Ti:Sa laser is that we want to show how to remotely synchronize an arbitrary color laser and how the laser's inherent jitter can affect the synchronization performance. In Fig. 7, the same master laser as in Sections 2 and 3 was used, and its repetition rate was locked to an RF reference to reduce its drift below ~200 Hz. The slave laser, is a home-built Ti:Sa Kerr-lens mode-locked laser operating at 800-nm center wavelength and 1.0833-GHz repetition rate. Then the output of the master laser was split into two separate timing links. Timing link 1 consisted of a 3.5-km polarization-maintaining (PM) dispersion-compensated fiber spool, a PM fiber stretcher, and a fiber-coupled motorized delay line with 560-ps range. Similarly, the components of timing link 2 included a 1.2-km PM fiber spool, a PM fiber stretcher, and a free-space motorized stage with 100-ps range. At the end of each link, there was a fiber-coupled mirror reflecting 10% of the optical power back to the link input. Here, a bidirectional erbium-doped fiber amplifier (EDFA) was also used to provide sufficient power for the back-propagating signal and the link output required for link stabilization and remote synchronization, respectively. At the link inputs, the round-trip pulses were combined with newly emitted ones in one-color (OC)-BOCs. OC-BOCs operate at 1554-nm wavelength and realize the cross-correlation with the birefringence between two orthogonally polarized input pulses. OC-BOCs measured the propagation delay fluctuations in the links and generated error voltages, which controlled the fiber stretchers and the motorized delays to compensate for fast jitter and long-term drifts, respectively. The Ti:Sa laser was placed at the output location of the timing links. As the master laser and Ti:Sa laser operate at different central wavelengths, two two-color BOCs (TC-BOCs) [58,59] were built between each link output and the Ti:Sa laser output. Both of the TC-BOCs were realized with type-I sum-frequency generation between 800-nm and 1550-nm central wavelengths in a beta-barium borate (BBO) crystal. TC-BOC1 synchronized the Ti:Sa laser with link 1 output by tuning the repetition rate via its intracavity PZT mirror. Finally, the free-running TC-BOC2 evaluates the timing precision between the synchronized Ti:Sa laser and timing link 2 output.

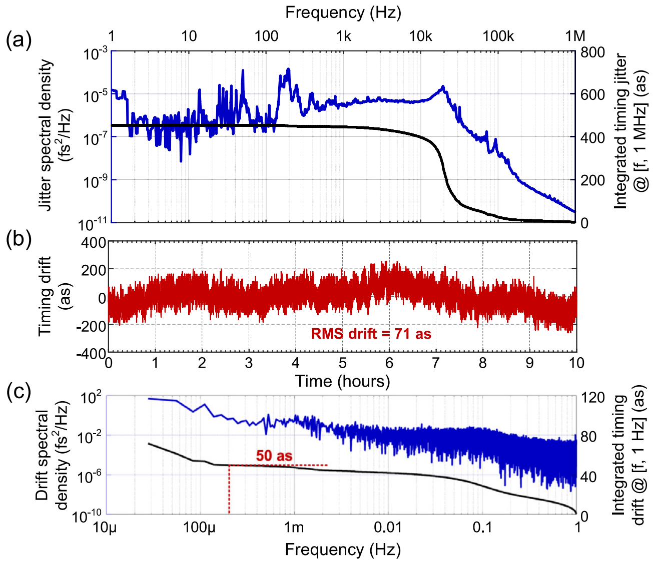

Fig. 6. Local optical–optical synchronization measurement results. (a) Out-of-loop jitter spectrum; (b) long-term timing drift (sampling rate: 2 Hz); (c) timing drift spectrum.

Fig. 8(a) shows the out-of-loop timing drift between the remotely synchronized Ti:Sa laser and timing link 2 output. We were able to keep the complete system synchronized for 8 h continuously, which is limited by the PZT range of the Ti:Sa laser. The observed drift is only 25-fs peak-to-peak and 3.65 fs RMS for the complete duration without any excess locking volatility. We also calculated the relative timing instability (i.e., timing error in terms of overlapping Allan deviation) from the drift data to investigate the system behavior for different averaging times. As Fig. 8(b) illustrates, the relative timing instability is only 1.2×10^{-15} in 1-s averaging time (τ) and falls to 3.36×10^{-19} at 10,000 s following a deterministic slope very close to τ^{-1}.

The timing jitter spectral density for offset frequencies larger than 1 Hz was measured with a baseband analyzer, which Fourier transformed the TC-BOC2 output. The red curve in Fig. 8(c) shows the out-of-loop jitter between the remotely synchronized Ti:Sa laser and timing

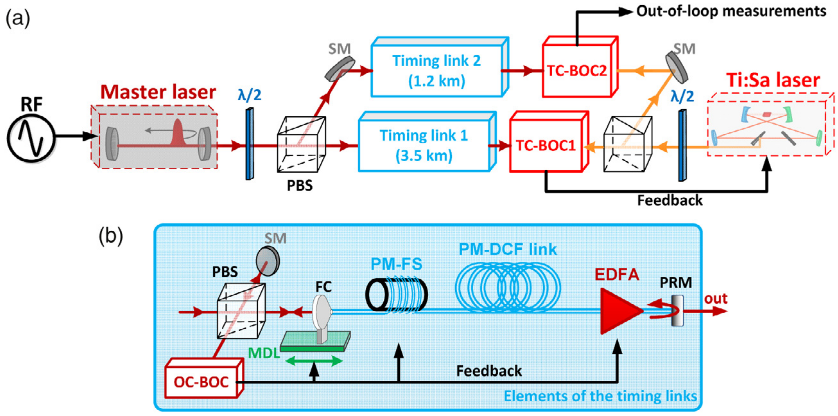

Fig. 7. [57](a) Experimental setup for the synchronization of the Ti:Sa laser on a timing link network with a total length of 4.7 km. (b) Individual elements of the timing stabilized fiber links. Abbreviations: RF: RF reference; FC: fiber collimator; MDL: motorized delay line; PM-FS: polarization-maintaining fiber stretcher; PM-DCF: PM dispersion-compensated fiber; EDFA: bidirectional erbium-doped fiber amplifier; PRM: partially reflecting fiber mirror.

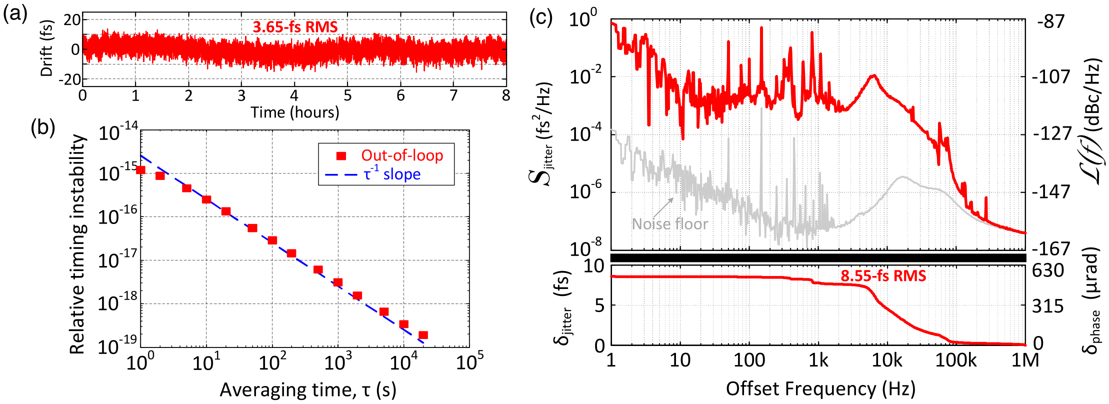

Fig. 8. [57] Out-of-loop measurements between the remotely synchronized Ti:Sa laser and timing link 2 output. (a) Timing drift below 1 Hz. (b) Calculated relative timing instability from the drift data. (c) Jitter spectral density S_{jitter} and its integrated jitter δ_{jitter}; right axes: equivalent SSB phase noise $\mathcal{L}(f)$ and its integrated phase δ_{phase} scaled to a 10-GHz carrier frequency. The gray curve shows the noise floor of the free-running TC-BOC2. (For interpretation of the references to color in this figure legend, the reader is referred to the web version of this article.)

link 2 output. The integrated jitter for 1 Hz–1 MHz is 8.55 fs RMS corresponding to a phase error of 0.5 mrad for a 10-GHz carrier.

5. Timing jitter noise analysis

5.1. Link-induced timing drift and jitter

Using the setup in Fig. 7, the technical noise sources of the timing synchronization system can be targeted. In Fig. 7(b), long-range compensation is performed by a motorized delay line with long free-space delay arms; e.g., a 10-cm range is required to correct for ±1.5-K temperature change in a 3.5-km link. Movement of the delay stage introduces inevitable beam misalignments that cause link power fluctuations. These fluctuations induce temporal shifts in the pulses' center-of-gravity (COG) through a composite effect of link residual second-order dispersion (SOD), third-order dispersion (TOD) and nonlinearities. Although a COG shift appears as a deterministic shift in the zero-crossing position of the in-loop BOC characteristic (i.e., the BOC output voltages with respect to the initial delay of the two input pulses), the link stabilization feedback will unknowingly track this shift and erroneously introduce it into the link path, causing a timing error at the link output.

To confirm this link-induced effect, we performed simulations using typical parameters from the experiments. Self-phase modulation, self-steepening and the Raman effect are considered in the link. Both the nonlinear Schrödinger equation [60] for the link transmission and the coupled field equations [61] for the SFG process in the BOC were solved using the split-step Fourier method with adaptive step length. The BOC characteristic was calculated for each round-trip link pulse against a new laser reference pulse. The timing offset of the zero-crossing position in the BOC characteristic was identified as timing error. The parameters B2/B3 were used to represent the link residual SOD/TOD normalized by the SOD/TOD of 1-m standard PM 1550 fiber. Fig. 9(a) shows that residual TOD can induce up to 5 fs timing error for +8-dBm link power with ±5% fluctuations. Fig. 9(b) indicates that +10-dBm link power is the threshold before significant amplitude-to-timing conversion occurs due to severe nonlinear pulse distortions that may result in 4 fs of timing error from ±5% power fluctuations.

In our experiments, the timing links were constructed employing a section of standard PM 1550 fiber, followed by a section of PM dispersion compensating fiber. Due to a little difference between the ratios of SOD to TOD coefficient in each fiber, when the SOD of a 3.5-km link was completely eliminated, 26-m worth of TOD from PM 1550 would remain uncompensated. Based on Fig. 9(a), this residual TOD can introduce a drift of at least 2 fs for ±5% link power fluctuations. In order to eliminate these power-fluctuations-induced drifts, the link power must be stabilized. As shown in Fig. 7(b), this can be realized by sending the third feedback signal to the PM-EDFA to adjust its pump current.

Besides the long-term drifts, the fast jitter of an optical pulse train can also be enhanced during fiber link transmission. We also developed a model to investigate this effect. In the model, the master equation of a fast-saturable-absorber mode-locked laser was solved using the fourth-order Runge–Kutta in the interaction picture (RK4IP) method [62]. Laser timing jitter was generated by adding amplified spontaneous emission

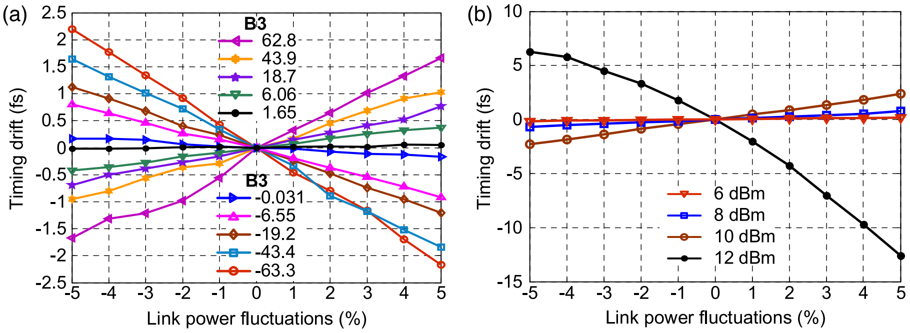

Fig. 9. [27] Timing drift introduced by link power fluctuations (in (a), the input power is +8 dBm and B2 = −0.13; in (b), B2 = −0.13 and B3 = 18.7).

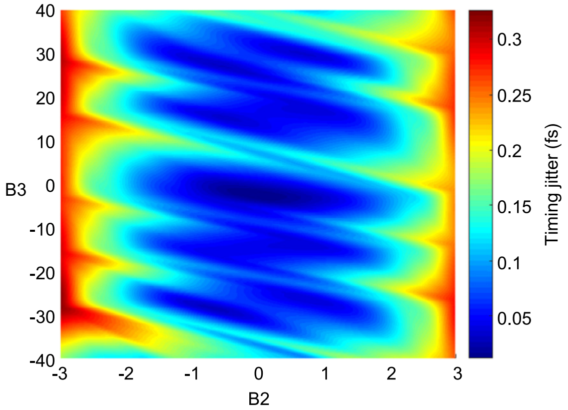

Fig. 10. Link-induced Gordon–Haus timing jitter for different B2/B3 values.

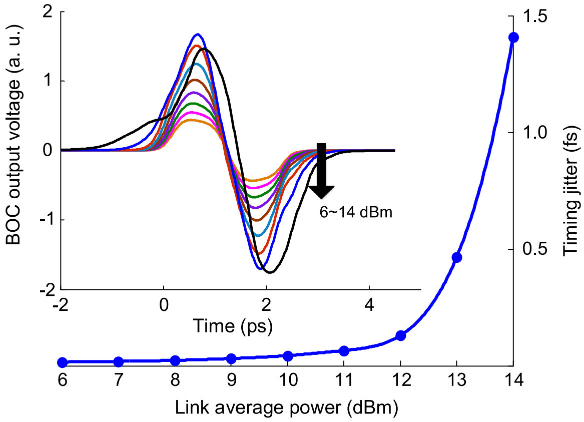

Fig. 11. [27] Link-induced timing jitter due to nonlinear effects in the fiber.

(ASE) noise during each iteration of RK4IP, whose amount corresponds to the measured jitter of the master laser in Section 2. The calculation was repeated for a train of laser pulses in the presence of pulse timing jitter and each pulse was solved by similar procedures in the link-induced drift simulation.

In Fig. 10, pulse center-frequency fluctuations are converted into timing jitter via residual SOD and TOD. This jitter contribution, often called Gordon–Haus jitter [63], can amount to 0.15 and 0.3 fs for uncompensated SOD equivalent to 2 and 3 m of standard PM fiber, respectively.

In Fig. 11, spontaneous emission noise is converted into timing jitter and its impact is further enhanced by link nonlinearities. The introduced jitter is bounded at 0.13 fs for average power levels below +12 dBm (corresponding to a pulse peak power of $P_{\text{peak}} = 430$ W) but escalates to 1.4 fs at +14 dBm ($P_{\text{peak}} = 682$ W). This jitter needs to be carefully minimized in practice because it easily reaches the fs-level before a visible distortion of the BOC characteristic can be observed, as shown in the inset of Fig. 11.

5.2. Feed-back model of Ti:Sa synchronization

As there are four BOCs and numerous locking elements used in Fig. 7, we perform a comprehensive feedback loop analysis to identify the factors influencing the observed jitter. Fig. 12 shows the feedback flow diagrams of each BOC-based timing measurement. In the feedback models of the timing links (Fig. 12(a) and (c)), the timing jitter of the link J_I is detected by the BOC and converted to a voltage signal by the BOC transfer function H_{BOC}. Then the BOC signal is amplified by H_{BPD} with the detector noise E_{BOC}. The BPD signal is fed to the PI controller H_{PI} in a negative feedback configuration. The output of the PI controller together with its electronic noise E_{PI} is amplified and converted to a jitter value J_F by the fiber stretcher H_{PZT}, which acts as a compensating jitter to maintain the lock. Since we perform error analysis upon round-trip link propagation, delayed copies of the compensation jitter J_F, master laser's inherent jitter J_M and the environmental jitter imposed on the link J_E are also added to the link jitter beside the original sources. A round-trip link delay $2\tau_L$ is considered for J_F and J_M, whereas only a one-way link delay τ_L is applied to J_E as it already includes one-way integrated environmental jitter by its definition.

The feedback flow for the remote synchronization of the Ti:Sa laser is given in Fig. 12(b). Four jitter sources, environmental jitter $J_{E,L1}$, compensation jitter of timing link 1 $J_{F,L1}$, the inherent jitter of the master and the slave laser J_M, and J_S need to be considered. Then again, one-way link delay must be applied to the inherent jitter of the master laser and to the link compensation jitter because they are actuated at the link input location.

Based on this model, we can obtain the out-of-loop timing jitter of the complete system:

$$\overline{J_O^2} = |C_M|^2 \overline{J_M^2} + |C_S|^2 \overline{J_S^2} + |C_{E,L1}|^2 \overline{J_{E,L1}^2} + |C_{E,L2}|^2 \overline{J_{E,L2}^2} + |C_{N,S}|^2 \overline{J_{N,S}^2} + |C_{N,L1}|^2 \overline{J_{N,L1}^2} + |C_{N,L2}|^2 \overline{J_{N,L2}^2} \tag{3}$$

where

$$C_M = \frac{(1+2H_{L2})\exp(-s\tau_{L2})}{1+H_{L2}(1+\exp(-2s\tau_{L2}))} - \frac{1}{1+H_S}\frac{(1+2H_{L1})\exp(-s\tau_{L1})}{1+H_{L1}(1+\exp(-2s\tau_{L1}))} \tag{4}$$

$$C_S = \frac{1}{1+H_S} \tag{5}$$

$$C_{E,L1} = -\frac{1}{1+H_S}\frac{1+H_{L1}\left[1-\exp(-s\tau_{L1})\right]}{1+H_{L1}\left[1+\exp(-2s\tau_{L1})\right]} \tag{6}$$

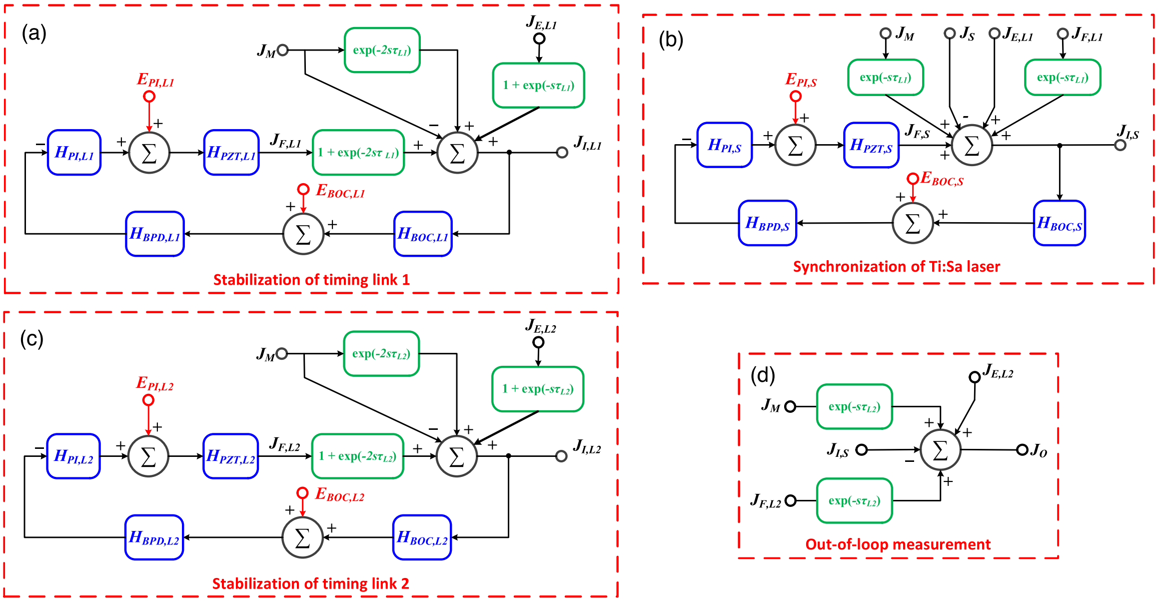

Fig. 12. [57] Feedback model for the setup of Fig. 7: (a) stabilization of timing link 1, (b) remote synchronization of the Ti:Sa laser via timing link 1, (c) stabilization of timing link 2, and (d) out-of-loop jitter measurement between the Ti:Sa laser and timing link 2. J_E: total environmental jitter imposed on the link for one-way travel; J_I: timing jitter detected by the in-loop BOC; J_F: equivalent jitter generated by the feedback loop to maintain the lock; J_O: out-of-loop jitter between the Ti:sSa laser and timing link 2 output; τ: one-way fiber link travel time, $s = j\omega$: complex frequency. Subscripts $L1$, $L2$, and S after each abbreviation refer to timing link 1, timing link 2 and the Ti:Sa laser, respectively.

$$C_{E,L2} = \frac{1 + H_{L2}\left[1 - \exp\left(-s\tau_{L2}\right)\right]}{1 + H_{L2}\left[1 + \exp\left(-2s\tau_{L2}\right)\right]} \tag{7}$$

$$C_{N,S} = -\frac{H_S}{1 + H_S} \tag{8}$$

$$C_{N,L1} = -\frac{1}{1 + H_S}\,\frac{H_{L1}\exp\left(-s\tau_{L1}\right)}{1 + H_{L1}\left[1 + \exp\left(-2s\tau_{L1}\right)\right]} \tag{9}$$

$$C_{N,L2} = \frac{H_{L2}\exp\left(-s\tau_{L2}\right)}{1 + H_{L2}\left[1 + \exp\left(-2s\tau_{L2}\right)\right]}. \tag{10}$$

During the experiment, we have observed that the measured out-of-loop jitter is highly sensitive to the feedback parameters of TC-BOC1 lock (i.e., synchronization of the Ti:Sa laser to the output of timing link 1). With the help of our feedback model, we can provide evidence for this observation by calculating the transfer coefficients for varying TC-BOC1 feedback gain (Fig. 13(a)–(g)). Except for the environmental noise on timing link 2 and the electronic noise of its stabilization (Fig. 13(d) and (g)), all other transfer coefficients are influenced by the synchronization of the Ti:Sa laser. By increasing the TC-BOC1 feedback gain, we can suppress the excess noise coming from the inherent jitter of the Ti:Sa laser, environmental disturbances imposed on timing link 1 and electronic jitter of its stabilization (see Fig. 13(b), (c) and (f)). This is highly intuitive because higher feedback gain achieves ideally tighter synchronization between the link output and the Ti:Sa laser. However, excess gain causes noise amplification peaks appearing around the PZT resonance of the Ti:Sa laser (Fig. 13(b), (c) and (f)) and introduces more electronic noise from the TC-BOC1 lock (Fig. 13(e)).

Fig. 13(a) confirms once more that it is vital to have a master laser with low inherent jitter, since it is transferred to the output entirely, even with amplification around the PZT resonance of its intracavity mirror. Fig. 13(d) shows that the environmental jitter on timing link 2 is well suppressed below 20 kHz. However, one has to pay attention to the electronic noise coming from its stabilization as it is transferred partially to the output by the feedback (Fig. 13(g)). Now that we have calculated the transfer coefficients, we can determine the jitter spectral densities in Eq. (3) and compare the results with the measured out-of-loop jitter. We obtain the environmental jitter imposed on the links ($\overline{J^2_{E,L1}}$ and $\overline{J^2_{E,L2}}$) experimentally by simply measuring their unlocked OC-BOC output voltage with a baseband analyzer. We use the experimental data from Section 2 for the master laser's inherent timing jitter ($\overline{J^2_M}$), whereas we estimate the inherent timing jitter of the Ti:Sa laser ($\overline{J^2_S}$) by doing another local jitter characterization experiment similar to that in Fig. 2 (replacing the slave laser with a Ti:Sa laser and the BOC with a TC-BOC). Finally, we estimate the electronic jitter terms ($\overline{J^2_{N,S}}$, $\overline{J^2_{N,L1}}$ and $\overline{J^2_{N,L2}}$) arising from the TC-BOC1, OC-BOC1 and OC-BOC2 locks respectively using a simple operational amplifier noise model.

Fig. 14(a) shows the simulation results of individual jitter contributions for offset frequencies from 100 Hz to 1 MHz where the low frequency limit is set by the free-running jitter of the master laser, which can be resolved down to 100 Hz. The inherent jitter of the Ti:Sa laser is by far the largest noise factor with 8.19-fs integrated jitter (dark blue curve). This result points out that it is imperative to pay considerable attention to the low noise properties of the slave lasers before employing them in timing synchronization applications requiring highest precision.

The inherent jitter of the master laser also plays an important role with 1.67-fs total jitter (light blue curve in Fig. 14(a)). Its contribution becomes more noticeable for offset frequencies below 200 Hz, which justifies the stabilization of its repetition rate with a low-noise RF source. However, one has to maintain a relatively low locking bandwidth here, as the master laser surpasses the RF source in terms of low-noise performance for higher offset frequencies.

Large feedback gain in the link stabilization helps to suppress the environmental noise on the fibers; however, one has to pay attention to the PZT resonances of the fiber stretchers. As can be seen from the dark green curve in Fig. 14(a), the environmental jitter imposed on timing link 1 accumulates 1.5-fs jitter due to the excess noise around 18 kHz caused by its PZT resonance. We can appreciate the advantage of low noise floors provided by the BOCs once more, since the least dominant jitter contributions in our system are the electronic noise coming from the feedback elements with a total integrated jitter below 0.3 fs.

Finally, we compare the sum of all individual jitter spectral densities with the out-of-loop measurement (Fig. 14(b)). The experiment and the simulation agree very well with each other as the simulation estimates 8.49 fs RMS total integrated jitter, whereas the experiment shows 8.51 fs RMS for 100 Hz–1 MHz. It even reveals many specific jitter structures such as electronic noise spurs below 2 kHz. However, there are some deviations between the two spectra for offset frequencies 5 kHz–25 kHz. We suspect that they originate from the imperfect estimation of the PZT transfer function of the Ti:Sa cavity mirror. The simulation results can be

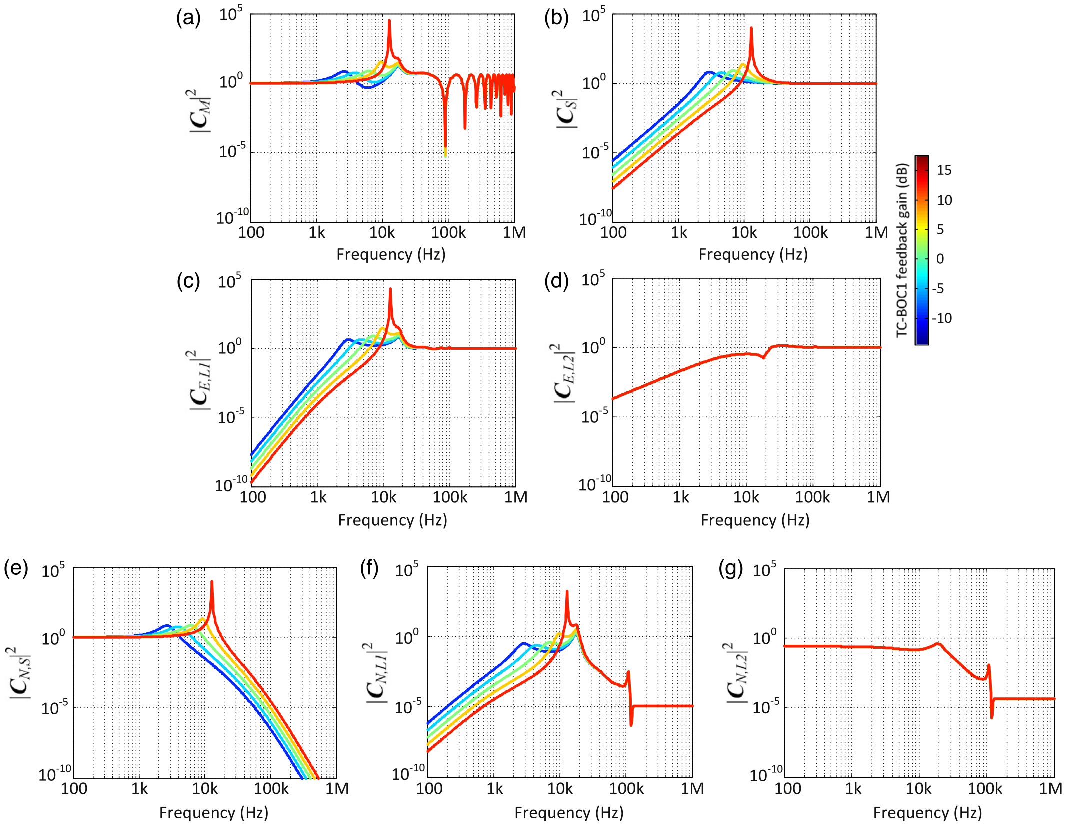

Fig. 13. [57] Calculated transfer coefficients in Eq. (3) for varying TC-BOC1 feedback gain. Coefficients are given as following: (a) master laser's inherent jitter; (b) slave laser's inherent jitter; environmental noise imposed on (c) timing link 1 and (d) timing link 2; electronic feedback noise from (e) TC-BOC1 lock, (f) OC-BOC1 lock, and (g) OC-BOC2 lock. The color map on the right-hand side is common for all figures. (For interpretation of the references to color in this figure legend, the reader is referred to the web version of this article.)

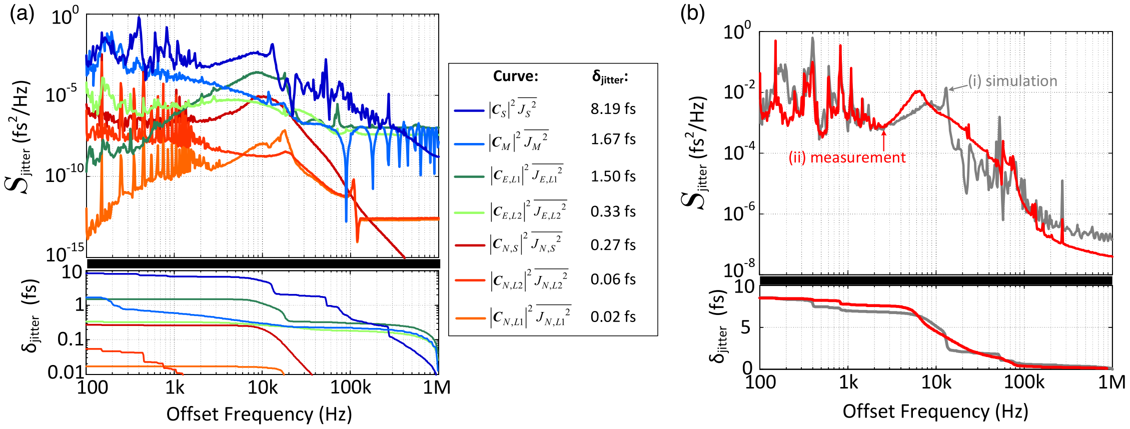

Fig. 14. [57] (a) Simulation results of individual jitter contributions. The legend on the right shows the color code of the jitter spectral densities and their integrated jitter from 100 Hz to 1 MHz. Integrated jitter in this graph is shown on a logarithmic scale. (b) Comparison between (i) the sum of all simulated jitter sources and (ii) the out-of-loop jitter measurement. (For interpretation of the references to color in this figure legend, the reader is referred to the web version of this article.)

improved even further by measuring the PZT voltage response around its resonance. Note that above 200 kHz, the simulation result is obscured by the environmental noise and master laser jitter measurements, which fall below the detector noise floor.

6. Laser–microwave network

Taking all the technical noise sources discussed above into account, an attosecond-precision laser–microwave network [27] is demonstrated using the setup shown in Fig. 15. The repetition rate of the master laser was locked to a microwave reference with a 10-Hz feedback bandwidth to suppress long-term drifts. The timing signal from the master laser was distributed through a network that contains two independent fiber links of 1.2-km and 3.5-km length operated in parallel. The link outputs were used to synchronize a remote laser (e.g., serving as a pump laser at the FEL end-station in Fig. 1) and a voltage-controlled oscillator (VCO) (e.g., serving as a microwave reference of the FEL linear accelerator in Fig. 1) simultaneously. Here the remote laser was the slave laser in Section 2 exhibiting very low inherent timing jitter. Polarization-noise-suppressed BOCs were used for each locking loop to eliminate the timing noise from the undesired pulse components [27] and a feedback precision of ∼2 as for the remote laser locking BOC is achieved with a low-noise BPD. The residual SOD and TOD of the links were compensated with additional dispersion-compensating fiber to suppress

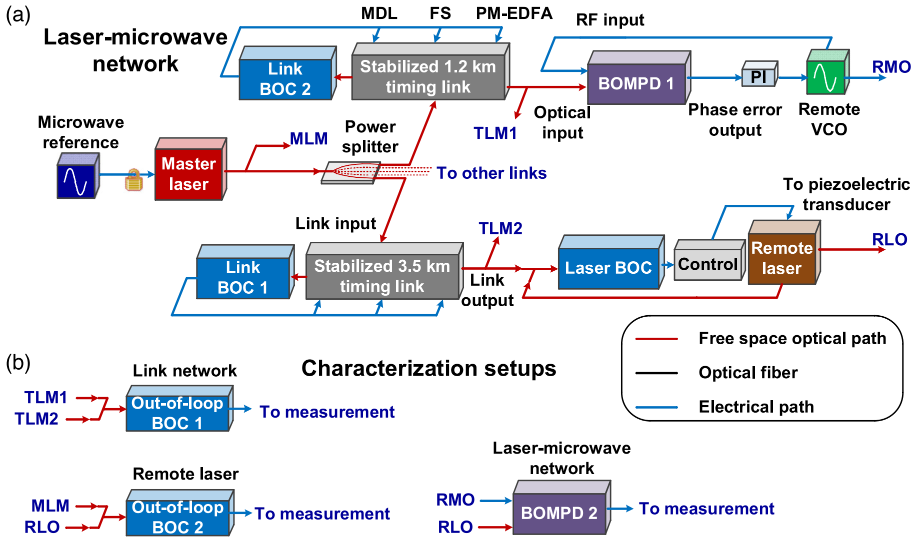

Fig. 15. [57] (a) Laser–microwave network (VCO, voltage-controlled oscillator); (b) Out-of-loop characterization setups.

the link-induced Gordon–Haus jitter and to minimize the output pulse durations for high signal-to-noise ratio (SNR) in the BOCs. The link power was adjusted to minimize the nonlinearity-induced jitter as well as to maximize the SNR for BOC locking. To eliminate power-fluctuation-induced drift, a feedback signal was sent to the EDFA to control its pump current. The free-space-coupled BOMPD [27] was employed for optical–microwave locking. Compared with the fiber-coupled approach [37,64], this new design can provide a >10× improvement for long-term timing stability. Besides, in contrast to other BOMPDs [65,66], its output error signal is insensitive to optical input power fluctuations.

Three characterization setups are adopted (Fig. 15(b)): two timing link monitoring signals (TLM1 and 2) were sent to an out-of-loop BOC to evaluate the link network performance; the master laser monitoring signal (MLM) and the remote laser output signal (RLO) were sent to another BOC to characterize the remote laser synchronization; finally, the remote microwave output (RMO) and RLO were compared with an out-of-loop BOMPD. The third setup is of great significance since it directly measures the true relative timing jitter between a remotely-synchronized mode-locked laser and a microwave source.

The measurement results are shown in Figs. 16–18. Stabilization of the 4.7-km link network is operated continuously for 52 h. The residual timing drift between TLM1 and 2 below 1 Hz amounts to only 200 as RMS (Fig. 16, red curve). The relative timing drift instability is 2×10^{-17} at 1 s averaging time τ and reduces to 2×10^{-20} at $\tau = 10^4$ s (Fig. 17, red circles). The total integrated timing jitter from 6 μHz to 1 MHz is only 580 as (Fig. 18, red curve).

Remote laser synchronization is achieved successfully for over 44 h without interruption. The residual timing drift is less than 100 as RMS (Fig. 16, blue curve), which is an order-of-magnitude improvement over previous results [47], and corresponds to a relative timing instability of 9×10^{-22} at 10^5 s (Fig. 17, blue triangles). The integrated jitter is only 200 as in the range of 7 μHz–1 kHz and 680 as for 7 μHz–1 MHz (Fig. 18, blue curve).

Finally, the whole laser–microwave network shows an unprecedented long-term precision of 670 as RMS out-of-loop drift over 18 h (Fig. 16, black curve). Compared with previous frequency-comb-based microwave transfer results [67], this setup includes an additional fiber link and a remote laser synchronization system, yet it still achieves more than an order-of-magnitude improvement. The relative timing jitter between the two remotely synchronized devices within the full frequency range from 15 μHz to 1 MHz is only 950 as RMS (Fig. 18, black curve).

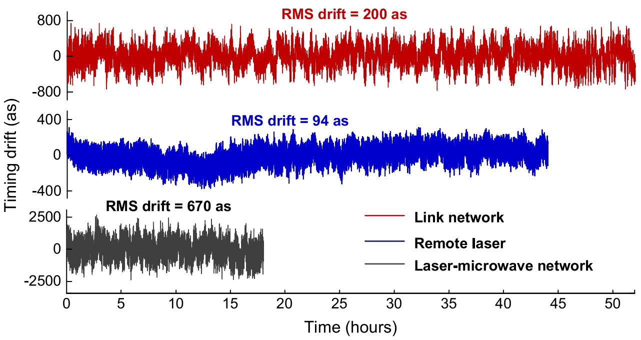

Fig. 16. [57] Long-term timing drift results for the laser–microwave network. (For interpretation of the references to color in this figure legend, the reader is referred to the web version of this article.)

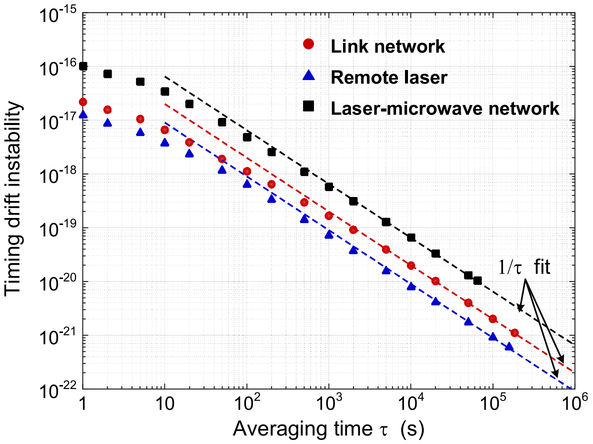

Fig. 17. [57] Timing drift instability (Allan deviation) of the laser–microwave network versus averaging time τ. Fits with τ^{-1} slope are shown. (For interpretation of the references to color in this figure legend, the reader is referred to the web version of this article.)

7. Integrated BOC and its measurement limit

Although the laser–microwave network in Fig. 15 already meets the strict timing requirement of next generation FELs, there is still a lot of

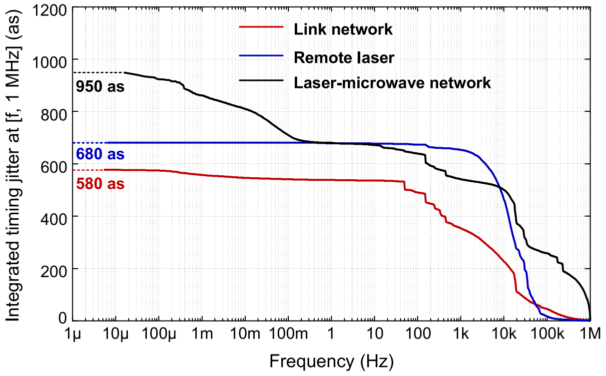

Fig. 18. [57] Integrated timing jitter of three characterization setups in the laser–microwave network. (For interpretation of the references to color in this figure legend, the reader is referred to the web version of this article.)

room to make the scheme more robust, power efficient and closer to the quantum limit. One solution toward this goal is to introduce integrated components. At this point a waveguide BOC was fabricated using ion-exchanged waveguides in potassium titanyl phosphate (KTiOPO$_4$), which was chosen because of its nonlinear optical properties, high-power handling, and wide acceptance bandwidth [68–70].

In order to characterize the performance of the integrated BOCs in the timing distribution system, we built an experimental setup as shown in Fig. 19. The master laser operated with a 200 MHz repetition rate, 100 fs pulse width, 1565 nm center wavelength. The repetition rate of the master laser was locked to a microwave reference (Agilent E8257D) to reduce its timing drift below 10 Hz. The laser output signal was separated into two paths for in-loop locking and out-of-loop measurement, respectively. The in-loop part was further divided into reference and link path pulses. The reference path lengths were set as short as possible (∼4 cm) to minimize timing errors introduced by environmental noise.

To assure that the forward and backward link transmission accumulates the same amount of jitter, the link pulse must travel along the same polarization axis during round-trip propagation. Therefore, a 45°Faraday rotator before the fiber link is necessary to introduce a 90°round-trip polarization rotation to direct the reflected link pulse toward the integrated BOC1. The 1.2-km PM link was constructed with a section of standard PM 1550 fiber, followed by a section of PM dispersion compensating fiber. Because the ratios of dispersion coefficients between the two fibers for SOD and TOD are a little different, if the SOD of the 1.2-km link was completely eliminated, 9-m worth of TOD from PM 1550 would be uncompensated. Due to the residual TOD, pulse durations of ∼200 fs were obtained at the link output.

After the link was stabilized, the link output pulses were combined with the original master laser pulses and sent into the integrated BOC2 to measure the residual timing jitter. The output voltage of BOC2 was first filtered by a 1-Hz RC filter and then sampled by a DAQ card, with 2-Hz sampling rate, so only the timing drift data below 1 Hz was recorded.

The detectors in the integrated BOCs are Thorlabs pigtailed silicon PIN photodiodes FDSP625. With 100 Ω load resistance R_{load}, 3 V reverse voltage, and 0.5 nA dark current (I_d), the photodiode's bandwidth is larger than 1 GHz. The output current of the two photodiodes are amplified by a transimpedance amplifier (TIA) SRS 570, which works in the low noise mode, i.e., most of the gain is allocated in the front end of the instrument to decrease the magnitude of Johnson noise at the output. With a gain (G) of 10^6V/A, the 3-dB bandwidth of the TIA is 200 kHz, and the current noise I_{TIA} is 600 fA/Hz$^{1/2}$. The total noise floor of the BOC is decided by the electronic noise V_E and shot noise V_S:

$$V_N = \sqrt{V_E^2 + V_S^2}. \tag{11}$$

The shot noise is obtained from the detected photocurrent I_s:

$$V_S = \sqrt{2}G\sqrt{2eI_s} \tag{12}$$

where e is the electron charge. And the electronic noise is contributed by the photodiode's thermal noise I_{th}, dark noise I_{dark} and the TIA's

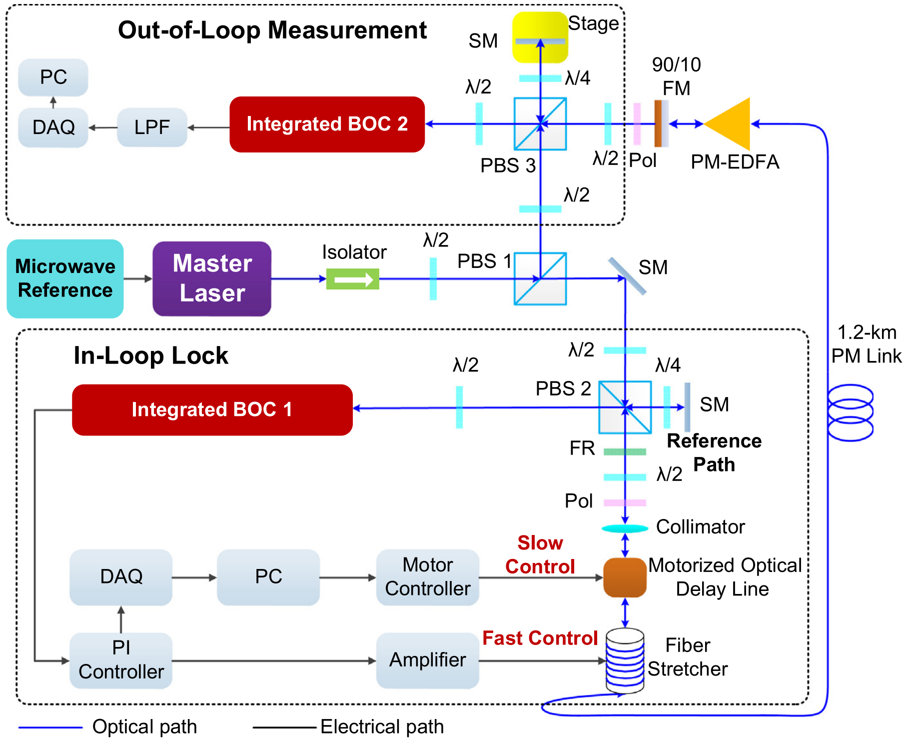

Fig. 19. Timing distribution setup for testing the integrated BOC device. FR: 45°Faraday rotator; Pol: polarizer; 1.2-km PM Link: 1.2-km PM dispersion compensated fiber link; 90/10 FM: 90/10 transmission/reflection fiber mirror; LPF: 1-Hz low pass filter.

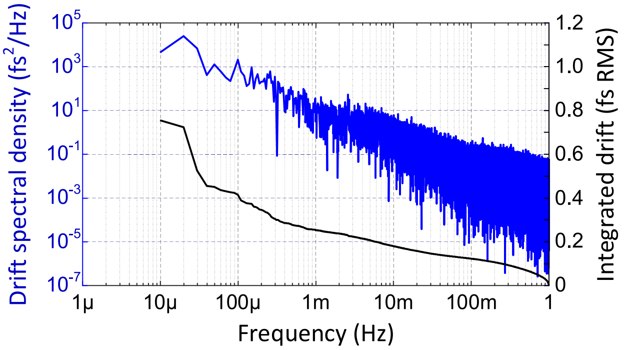

Fig. 20. Timing drift spectrum for integrated BOC.

current noise I_{TIA}:

$$V_E = G\sqrt{2I_{th}^2 + 2I_{dark}^2 + I_{TIA}^2} \tag{13}$$

$$I_{th} = \sqrt{\frac{4k_B T}{R_{load}}} \tag{14}$$

$$I_{dark} = \sqrt{2eI_d} \tag{15}$$

where k_B is Boltzmann constant and T is the environmental temperature. For in-loop and out-of-loop BOC, substituting the experimental values, we have $V_{N1} \approx 9.23\ \mu\mathrm{V/Hz}^{1/2}$ and $V_{N2} \approx 9.17\ \mu\mathrm{V/Hz}^{1/2}$.

The measured BOC timing sensitivity of in-loop and out-of-loop BOC around the zero-crossing point are 8.6 fs/mV and 4.4 fs/mV, respectively. Using the calculated noise values above, the feedback precision of the in-loop BOC is 0.1 fs (10 kHz feedback bandwidth), and the out-of-loop measurement precision for timing drift (<1 Hz) is 2 as.

The link locking was continuously operated over 28 h, exhibiting an RMS drift of 0.75 fs. During this period, more than 20 ps delay has been compensated by the motorized delay line. The timing drift spectrum is calculated and shown in Fig. 20. From the integrated drift curve, it can be seen that most of the drift comes from the contribution below 1 mHz. The integrated drift from 1 mHz to 1 Hz is only about 0.25 fs. The main noise source for the long-term drift above the one-hour scale is coming from the free-space optics in Fig. 19. By employing the thermal stabilization scheme in Fig. 5, this noise source can be substantially reduced (>90 times).

The main advantage of using integrated BOCs is on the power budget. In the experiment, the link input power is 6 dBm, which is the minimum power level to suppress the ASE noise of the EDFA at the end of the link. For this power level, to obtain the sensitivity of 8.6 fs/mV, the reference power is about 12 dBm. If a free-space BOC was used, the required reference power would be at least 6 dB higher. So to maintain the same locking precision, the integrated BOC can save >47 mW power per link. For a typical mode-locked laser with 200 mW average power, the integrated BOCs can support 10 links simultaneously without preamplifier, while free-space BOCs can only support three. Furthermore, the robustness and ease of implementation of integrated BOCs also make it more practical then the free-space version, which has many alignment-related challenges.

Before concluding this section, it is necessary to evaluate the measurement limit of the integrated BOC. Based on Eq. (11), the timing precision of a BOC is either limited by the detector's electronic noise or the optical shot noise of SFG. Besides, the timing standard quantum limit of an ultrashort pulse is defined as [71]:

$$\left\langle \hat{T}^2 \right\rangle \geq \frac{\Delta t^2}{N} \tag{16}$$

where Δt is the pulse width and N is the average photon number per pulse. We use typical experimental parameters and assume that the two input optical pulse trains of a BOC have the same average power, which are given on the horizontal axis of Fig. 21. Using the free-space-coupled BOC, the shot noise begins to surpass the electronic noise when the input power is above 200 mW (blue/red dotted curves in Fig. 21). By replacing the free-space BOC with the integrated version, the SFG efficiency can be increased by at least ten times, as a result the shot/electronic noise floor can be further decreased by 10/20 dB (blue/red solid curves in Fig. 21). The timing standard quantum limit is also shown as the black curve in Fig. 21. The integrated BOC becomes quantum-limited at a much lower power level (~50 mW) compared with the free-space version.

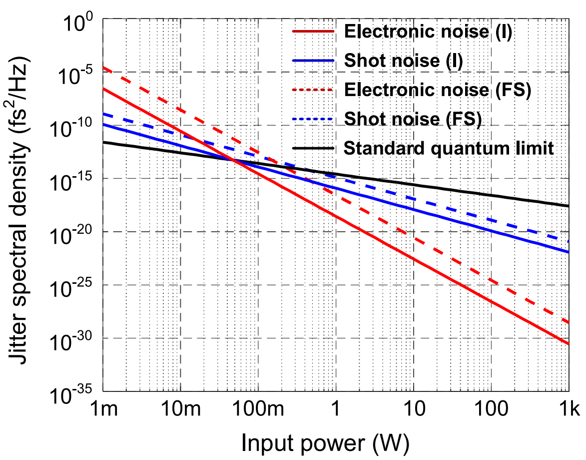

Fig. 21. Noise floor of BOC at different input average power levels (I, integrated; FS, free space). Pulse width: 100 fs; Nyquist bandwidth: 100 MHz; SFG efficiency: $4 \times 10^{-2}\ \mathrm{W}^{-1}$ (I), $4 \times 10^{-3}\ \mathrm{W}^{-1}$ (FS); BOC sensitivity with 100 mW/100 mW input power: 20 mV/fs (I), 2 mV (FS); BPD responsivity: 0.6 A/W; BPD transimpedance gain: 1×10^3 V/A; BPD noise equivalent power: 7 pW/Hz$^{1/2}$. (For interpretation of the references to color in this figure legend, the reader is referred to the web version of this article.)

8. Conclusions

In summary, we have successfully achieved long-term-stable attosecond timing precision across a 4.7-km fiber link network between remote optical and microwave devices. For shorter link lengths (e.g., ~300 m), because of lower required link operational power and smaller residual link dispersion, a better timing precision can be expected. Our technique can be easily transferred to multi-wavelength-laser networks [72,73] and large-scale microwave networks with μrad precision [74]. By introducing the integrated BOC, the required power to operate each timing link is significantly decreased and one master laser can support >10 timing links simultaneously without a preamplifier. The sub-fs-precision timing synchronization system will enable next-generation FELs and other science facilities to operate with unprecedented timing precision thereby unfolding their full potential. This will drive new scientific efforts toward the making of atomic and molecular movies at the attosecond time scale, opening up many new research avenues in structural biology, drug development, chemistry, fundamental physics and material science.

Acknowledgments

This work was supported by the European Research Council under the European Union's Seventh Framework Program (FP/2007-2013)/ERC Grant Agreement No. 609920 and the Cluster of Excellence "The Hamburg Centre for Ultrafast Imaging – Structure, Dynamics and Control of Matter at the Atomic Scale" of the Deutsche Forschungsgemeinschaft; The US Department of Energy under Award Number DE-SC0011377.

References

[1] G. Dimitrakopoulos, P. Demestichas, Intelligent transportation systems, IEEE Veh. Technol. Mag. 5 (2010) 77.

[2] T. Ohanian, N. Phillips, Digital Filmmaking: The Changing Art and Craft of Making Motion Pictures, second ed., Focal Press, Burlington, MA, 2013, pp. 89–95.

[3] J. Laroche, Estimating tempo, swing and beat locations in audio recordings, in: IEEE Workshop on the Applications of Signal Processing to Audio and Acoustics, 2001, pp. 135-138.

[4] W. Shieh, C. Athaudage, Coherent optical orthogonal frequency division multiplexing, Electron. Lett. 42 (2006) 587.

[5] A. Khilo, et al., Photonic ADC: overcoming the bottleneck of electronic jitter, Opt. Express 20 (2012) 4454.

[6] J.D. Lindl, P. Amendt, R.L. Berger, S.G. Glendinning, S.H. Glenzer, S.W. Haan, R.L. Kauffman, O.L. Landen, L.J. Suter, The physics basis for ignition using indirect-drive targets on the National Ignition Facility, Phys. Plasmas 11 (2004) 339.

[7] G. Mourou, B. Brocklesby, T. Tajima, J. Limpert, The future is fibre accelerators, Nat. Photonics 7 (2013) 258.

[8] P.J. Napier, A.R. Thompson, R.D. Ekers, The very large array: Design and performance of a modern synthesis radio telescope, Proc. IEEE 71 (1983) 1295.

[9] J.F. Cliché, B. Shillue, Precision timing control for radioastronomy: maintaining femtosecond synchronization in the atacama large millimeter array, IEEE Control. Syst. 26 (2006) 19.

[10] D.R. DeBoer, R.G. Gough, J.D. Bunton, et al., Australian SKA pathfinder: A high-dynamic range wide-field of view survey telescope, Proc. IEEE 97 (2009) 1507.

[11] E. Middelberg, U. Bach, High resolution radio astronomy using very long baseline interferometry, Rep. Progr. Phys. 71 (2008) 066901.

[12] D. Dravins, T. Lagadec, P.D. Nuñez, Optical aperture synthesis with electronically connected telescopes, Nature Commun. 6 (2015) 6852.

[13] P.W. Graham, J.M. Hogan, M.A. Kasevich, S. Rajendran, New method for gravitational wave detection with atomic sensors, Phys. Rev. Lett. 110 (2013) 171102.

[14] S. Kolkowitz, I. Pikovski, N. Langellier, M.D. Lukin, R.L. Walsworth, J. Ye, Gravitational wave detection with optical lattice atomic clocks, Phys. Rev. D 94 (2016) 12403.

[15] B.P. Abbott, et al., Observation of gravitational waves from a binary black hole merger, Phys. Rev. Lett. 116 (2016) 061102.

[16] B.P. Abbott, et al., GW151226: Observation of gravitational waves from a 22-solar-mass binary black hole coalescence, Phys. Rev. Lett. 116 (2016) 241103.

[17] M. Altarelli, R. Brinkmann, M. Chergui, W. Decking, B. Dobson, S. Düsterer, G. Grübel, W. Graeff, H. Graafsma, J. Hajdu, XFEL: The European X-ray Free-Electron Laser, DESY, Technical Design Report, 2006.

[18] E. Allaria, et al., Highly coherent and stable pulses from the FERMI seeded free-electron laser in the extreme ultraviolet, Nat. Photonics 6 (2012) 699.

[19] P. Emma, et al., First lasing and operation of an ångstrom-wavelength free-electron laser, Nat. Photonics 4 (2010) 641.

[20] J. Stohr, Linac Coherent Light Source II (LCLS-II) Conceptual Design Report, SLAC, Design Report, No. SLAC-R-978, 2011.

[21] E. Prat, S. Reiche, Simple method to generate terawatt-attosecond X-ray free-electron-laser pulses, Phys. Rev. Lett. 114 (2015) 244801.

[22] C. Kupitz, et al., Serial time-resolved crystallography of photosystem II using a femtosecond X-ray laser, Nature 513 (2014) 261.

[23] H. Öström, et al., Probing the transition state region in catalytic CO oxidation on Ru, Science 347 (2015) 978.

[24] F. Calegari, D. Ayuso, A. Trabattoni, L. Belshaw, S. De Camillis, S. Anumula, F. Frassetto, L. Poletto, A. Palacios, P. Decleva, J.B. Greenwood, F. Martín, M. Nisoli, Ultrafast electron dynamics in phenylalanine initiated by attosecond pulses, Science 346 (2014) 336.

[25] S.K. Son, L. Young, R. Santra, Impact of hollow-atom formation on coherent x-ray scattering at high intensity, Phys. Rev. A 83 (2011) 033402.

[26] S.P. Hau-Riege, Photoelectron dynamics in X-ray free-electron-laser diffractive imaging of biological samples, Phys. Rev. Lett. 108 (2012) 238101.

[27] M. Xin, K. Şafak, M.Y. Peng, A. Kalaydzhyan, W. Wang, O.D. Mücke, F.X. Kärtner, Attosecond precision multi-km laser-microwave network, Light Sci. Appl. 6 (2017) e16187.

[28] C.W. Chou, D.B. Hume, T. Rosenband, D.J. Wineland, Optical clocks and relativity, Science 329 (2010) 1630.

[29] T.L. Nicholson, S.L. Campbell, R.B. Hutson, G.E. Marti, B.J. Bloom, R.L. McNally, W. Zhang, M.D. Barrett, M.S. Safronova, G.F. Strouse, W.L. Tew, J. Ye, Systematic evaluation of an atomic clock at 2×10^{-18} total uncertainty, Nature Commun. 6 (2015) 6896.

[30] D. Meiser, J. Ye, D.R. Carlson, M.J. Holland, Prospects for a millihertz-linewidth laser, Phys. Rev. Lett. 102 (2009) 163601.

[31] C. Hagemann, C. Grebing, C. Lisdat, S. Falke, T. Legero, U. Sterr, F. Riehle, M.J. Martin, J. Ye, Ultrastable laser with average fractional frequency drift rate below 5×10^{-19}/s, Opt. Lett. 39 (2014) 5102.

[32] T.K. Kim, Y. Song, K. Jung, C. Kim, H. Kim, C.H. Nam, J. Kim, Sub-100-as timing jitter optical pulse trains from mode-locked Er-fiber lasers, Opt. Lett. 36 (2011) 4443.

[33] A.J. Benedick, J.G. Fujimoto, F.X. Kärtner, Optical flywheels with attosecond jitter, Nat. Photonics 6 (2012) 97.

[34] T.R. Schibli, J. Kim, O. Kuzucu, J.T. Gopinath, S.N. Tandon, G.S. Petrich, L.A. Kolodziejski, J.G. Fujimoto, E.P. Ippen, F.X. Kärtner, Attosecond active synchronization of passively mode-locked lasers by balanced cross correlation, Opt. Lett. 28 (2003) 947.

[35] J. Kim, J. Chen, Z. Zhang, F.N.C. Wong, F.X. Kärtner, F. Loehl, H. Schlarb, Long-term femtosecond timing link stabilization using a single-crystal balanced cross correlator, Opt. Lett. 32 (2007) 1044.

[36] J. Kim, F.X. Kärtner, F. Ludwig, Balanced optical–microwave phase detectors for optoelectronic phase-locked loops, Opt. Lett. 31 (2006) 3659.

[37] M.Y. Peng, A. Kalaydzhyan, F.X. Kärtner, Balanced optical-microwave phase detector for sub-femtosecond optical-RF synchronization, Opt. Express 22 (2014) 27102.

[38] S. Foreman, A. Ludlow, M. Miranda, J. Stalnaker, S. Diddams, J. Ye, Coherent optical phase transfer over a 32-km fiber with 1 s instability at 10^{-17}, Phys. Rev. Lett. 99 (2007) 153601.

[39] I. Coddington, W.C. Swann, L. Lorini, J.C. Bergquist, Y. Le Coq, C.W. Oates, Q. Quraishi, K.S. Feder, J.W. Nicholson, P.S. Westbrook, S.A. Diddams, N.R. Newbury, Coherent optical link over hundreds of metres and hundreds of terahertz with subfemtosecond timing jitter, Nat. Photonics 1 (2007) 283.

[40] J. Kim, J.A. Cox, J. Chen, F.X. Kärtner, Drift-free femtosecond timing synchronization of remote optical and microwave sources, Nat. Photonics 2 (2008) 733.

[41] O. Lopez, A. Amy-Klein, M. Lours, C. Chardonnet, G. Santarelli, High-resolution microwave frequency dissemination on an 86-km urban optical link, Appl. Phys. B 98 (2010) 723.

[42] K. Predehl, G. Grosche, S.M.F. Raupach, S. Droste, O. Terra, J. Alnis, T. Legero, T.W. Hänsch, T. Udem, R. Holzwarth, H. Schnatz, A 920-kilometer optical fiber link for frequency metrology at the 19th decimal place, Science 336 (2012) 441.

[43] S. Schulz, I. Grguraš, C. Behrens, H. Bromberger, J.T. Costello, M.K. Czwalinna, M. Felber, M.C. Hoffmann, M. Ilchen, H.Y. Liu, T. Mazza, M. Meyer, S. Pfeiffer, P. Prędki, S. Schefer, C. Schmidt, U. Wegner, H. Schlarb, A.L. Cavalieri, Femtosecond all-optical synchronization of an X-ray free-electron laser, Nature Commun. 6 (2015) 5938.

[44] F.R. Giorgetta, W.C. Swann, L.C. Sinclair, E. Baumann, I. Coddington, N.R. Newbury, Optical two-way time and frequency transfer over free space, Nat. Photonics 7 (2013) 434.

[45] J.D. Deschênes, L.C. Sinclair, F.R. Giorgetta, W.C. Swann, E. Baumann, H. Bergeron, M. Cermak, I. Coddington, N.R. Newbury, Synchronization of distant optical clocks at the femtosecond level, Phys. Rev. X 6 (2016) 021016.

[46] M.Y. Peng, P.T. Callahan, A.H. Nejadmalayeri, S. Valente, M. Xin, L. Grüner-Nielsen, E.M. Monberg, M. Yan, J.M. Fini, F.X. Kärtner, Long-term stable, sub-femtosecond timing distribution via a 1.2-km polarization-maintaining fiber link: approaching 10^{-21} link stability, Opt. Express 21 (2013) 19982.

[47] M. Xin K. Şafak, M.Y. Peng, P.T. Callahan, F.X. Kärtner, One-femtosecond, long-term stable remote laser synchronization over a 3.5-km fiber link, Opt. Express 22 (2014) 14904.

[48] K. Şafak, M. Xin, P.T. Callahan, M.Y. Peng, F.X. Kärtner, All fiber-coupled, long-term stable timing distribution for free electron lasers with few-femtosecond jitter, Struct. Dyn. 2 (2015) 041715.

[49] R. Wilcox, J.M. Byrd, L. Doolittle, G. Huang, J.W. Staples, Stable transmission of radio frequency signals on fiber links using interferometric delay sensing, Opt. Lett. 34 (2009) 3050.

[50] J.M. Glownia, et al., Time-resolved pump-probe experiments at the LCLS, Opt. Express 18 (2010) 17620.

[51] R.P. Scott, C. Langrock, B.H. Kolner, High-dynamic-range laser amplitude and phase noise measurement techniques, IEEE J. Sel. Top. Quantum Electron. 7 (2001) 641.

[52] F. Quinlan, T.M. Fortier, H. Jiang, A. Hati, C. Nelson, Y. Fu, J.C. Campbell, S.A. Diddams, Exploiting shot noise correlations in the photodetection of ultrashort optical pulse trains, Nat. Photonics 7 (2013) 290.

[53] W. Sun, F. Quinlan, T.M. Fortier, J.-D. Deschenes, Y. Fu, S.A. Diddams, J.C. Campbell, Broadband noise limit in the photodetection of ultralow jitter optical pulses, Phys. Rev. Lett. 113 (2014) 203901.

[54] J. Kim, J. Chen, J. Cox, F.X. Kärtner, Attosecond-resolution timing jitter characterization of free-running mode-locked lasers, Opt. Lett. 32 (2007) 3519.

[55] J.A. Cox, A.H. Nejadmalayeri, J. Kim, F.X. Kärtner, Complete characterization of quantum-limited timing jitter in passively mode-locked fiber lasers, Opt. Lett. 35 (2010) 3522.

[56] Y. Song, C. Kim, K. Jung, H. Kim, J. Kim, Timing jitter optimization of mode-locked Yb-fiber lasers toward the attosecond regime, Opt. Express 19 (2011) 14518.

[57] K. Şafak, M. Xin, Q. Zhang, S. Chia, O.D. Mücke, F.X. Kärtner, Jitter analysis of timing-distribution and remote-laser synchronization systems, Opt. Express 24 (2016) 21752–21766.

[58] H. Li, L.-J. Chen, H.P.H. Cheng, J.E. May, S. Smith, K. Muehlig, A. Uttamadoss, J.C. Frisch, A.R. Fry, F.X. Kärtner, P.H. Bucksbaum, Remote two-color optical-to-optical synchronization between two passively mode-locked lasers, Opt. Lett. 39 (2014) 5325.

[59] G. Zhou, M. Xin, F.X. Kärtner, G. Chang, Timing jitter of Raman soliton, Opt. Lett. 40 (2015) 5105.

[60] G.P. Agrawal, Nonlinear Fiber Optics, fourth ed., Academic Press, Burlington, MA, 2013.

[61] J.C. Diels, W. Rudolph, Ultrashort Laser Pulse Phenomena, second ed., Academic Press, Burlington, MA, 2006.

[62] J. Hult, A fourth-order Runge–Kutta in the interaction picture method for simulating supercontinuum generation in optical fibers, IEEE J. Lightwave Technol. 25 (2007) 3770.

[63] J.P. Gordon, H.A. Haus, Random walk of coherently amplified solitons in optical fiber transmission, Opt. Lett. 11 (1986) 665.

[64] A. Kalaydzhyan, M.Y. Peng, M. Xin, K. Şafak, W. Wang, F.X. Kärtner, Optical-to-microwave synchronization with sub-femtosecond daily drift, in: Presented at 30th European Frequency and Time Forum (EFTF), York, UK, 2016.

[65] K. Jung, J. Kim, Sub-femtosecond synchronization of microwave oscillators with mode-locked Er-fiber lasers, Opt. Lett. 37 (2012) 2958.

[66] M. Lessing, H.S. Margolis, C.T.A. Brown, P. Gill, G. Marra, Suppression of amplitude-to-phase noise conversion in balanced optical-microwave phase detectors, Opt. Express 21 (2013) 27057.

[67] K. Jung, J. Shin, J. Kang, S. Hunziker, C. Min, J. Kim, Frequency comb-based microwave transfer over fiber with 7×10^{-19} instability using fiber-loop optical-microwave phase detectors, Opt. Lett. 39 (2014) 1577.

[68] A.H. Nejadmalayeri, F.N.C. Wong, T.D. Roberts, P. Battle, F.X. Kärtner, Guided wave optics in periodically poled KTP: quadratic nonlinearity and prospects for attosecond jitter characterization, Opt. Lett. 34 (2009) 2522.

[69] P.T. Callahan, K. Şafak, P. Battle, T.D. Roberts, F.X. Kärtner, Fiber-coupled balanced optical cross-correlator using PPKTP waveguides, Opt. Express 22 (2014) 9749.

[70] B. Jones, T. Hawthorne, P. Battle, K. Shtyrkova, M. Xin, P.T. Callahan, F.X. Kärtner, T. Roberts, Development of a waveguide-based optical cross-correlator for attosecond timing synchronization, Ultrafast Optics UFO XI, Jackson Hole, Wyoming USA, October 2017.

[71] V. Giovannetti, S. Lloyd, L. Maccone, Quantum enhanced positioning and clock synchronization, Nature 412 (2001) 417.

[72] K. Şafak, M. Xin, M.Y. Peng, F.X. Kärtner, Synchronous mode-locked laser network with sub-fs jitter and multi-km distance, in: Presented at Conference on Lasers & Electro-Optics (CLEO), San José, CA, USA, 2016, paper SM4H.2.

[73] K. Şafak, M. Xin, M.Y. Peng, F.X. Kärtner, Synchronous mode-locked laser network with 20th decimal timing precision, arXiv:1710.09591.

[74] W. Wang, A. Kalaydzhyan, K. Şafak, M. Xin, M.Y. Peng, K. Jung, J. Kim, F.X. Kärtner, High precision synchronization of a large-scale microwave network over stabilized fiber links, in: Presented at Conference on Lasers & Electro-Optics (CLEO), San José, CA, USA, 2016.